

Electronic Supplementary Information (ESI) for ChemComm.

This journal is © The Royal Society of Chemistry 2022

†Electronic Supporting Information (†ESI)

**2D Bimetallic Ni-Co Hydroxide Monolayer Cocatalyst for Boosting  
Photocatalytic H<sub>2</sub> Evolution**

Haiwei Su,<sup>a</sup> Xiaohui Yu,<sup>a</sup> Weikang Wang,<sup>\*b</sup> Lele Wang,<sup>a</sup> Hua Tang<sup>\*ac</sup>

and Qinqin Liu<sup>\*a</sup>

a. School of Materials Science and Engineering, Jiangsu University, Zhenjiang,  
Jiangsu, 212013, P. R. China

b. School of Environmental and Chemical Engineering, Jiangsu University of Science  
and Technology, Zhenjiang, Jiangsu, 212100, P. R. China

c. School of Environmental Science and Engineering, Qingdao University, Qingdao,  
266071, P. R. China

\*Corresponding authors:

Weikang Wang, E-mail: wangwk@issp.ac.cn

Hua Tang, E-mail: huatang79@163.com

Qinqin Liu, E-mail: qqliu@ujs.edu.cn

## 1. Experimental section

### 1.1 Chemicals.

Shanghai Aladdin Biochemical Reagent Co. provided urea and melamine. Nickel (II) acetate tetrahydrate ( $\text{Ni}(\text{CH}_3\text{COO})_2 \cdot 4\text{H}_2\text{O}$ ), Cobalt (II) acetate tetrahydrate ( $\text{Co}(\text{CH}_3\text{COO})_2 \cdot 4\text{H}_2\text{O}$ ), hydrochloric acid (HCl), ammonia ( $\text{NH}_3 \cdot \text{H}_2\text{O}$ ), ethylene glycol, Nickel (II) nitrate hexahydrate ( $\text{Ni}(\text{NO}_3)_2 \cdot 6\text{H}_2\text{O}$ ) and Cobalt (II) nitrate hexahydrate ( $\text{Co}(\text{NO}_3)_2 \cdot 6\text{H}_2\text{O}$ ) were purchased from Sinopharm Chemical Reagent Co. Anhydrous ethanol, triethanolamine (Sinopharm Chemical Reagent Co., Ltd.) and deionized water (18.2 M $\Omega$ , 300.6 K) were used in this work.

**1.2 Preparation of carbon nitride nanosheets (CN):** Specifically, 15 g of urea was placed in a 30 mL crucible and subsequently transferred to a muffle furnace followed by sintering three times. The first time was heated at a rate of 2°C/min and held for 4 h at 550°C. The second time was heated at a rate of 5°C/min and held at 550°C for 1 h. The second time was heated at a rate of 2°C/min and held at 550°C for 1 h. The final obtained yellowish powders were g-C<sub>3</sub>N<sub>4</sub> nanosheets (noted as CN).

**1.3 Preparation of tubular carbon nitride (TCN):** 5.0 g of urea and 0.4 g of melamine were mix and ground thoroughly for 20 min. After that, the mixture was sintered in a porcelain boat at 550°C for 4 h in a N<sub>2</sub> atmosphere with a heating rate of 5°C/min to obtain a light yellow powder (identified as TCN).

**1.4 Preparation of bulk carbon nitride nanosheets (BCN):** 15 g of urea was placed in a 30 mL crucible and subsequently transferred to a muffle furnace and then heated 550°C for 4 h.

**1.5 Preparation of protonated CN nanosheets (PCN):** 200 mg of CN were dissolved in 40 mL of a 10 M hydrochloric (HCl) acid solution and agitated for 12 h. The product was washed to neutral and then deposited in a vacuum oven at 70°C overnight and collected as PCN. Furthermore, PTCN and PBCN are obtained using this same procedure by replacing CN with TCN or BCN.

**1.6 Preparation of Ni-Co hydroxide monolayers/PCN hybrids (NiCo-HMs-x/PCN):** 75 mg of PCN was sonicated for 30 mins in a solution of 35 mL H<sub>2</sub>O and 5 mL anhydrous ethanol. After that, Co(CH<sub>3</sub>COO)<sub>2</sub>·4H<sub>2</sub>O and Ni(CH<sub>3</sub>COO)<sub>2</sub>·4H<sub>2</sub>O with the molar ratio of 2:1 were added, respectively. 1 mL of NH<sub>3</sub>·H<sub>2</sub>O was added dropwise following by an oil-bath treatment at 80°C for 2 h. The solution was transferred to a 50 mL Teflon-filled reaction vessel and kept at 80°C for 20 h, and followed by an oil-bath at 170°C for 3 h. The products were freeze-dried for 24 h after repeated water washes, and the gray samples were collected and labeled as NiCo-HMs-1/PCN, NiCo-HMs-2/PCN, NiCo-HMs-3/PCN and NiCo-HMs-4/PCN when the adding of Co(CH<sub>3</sub>COO)<sub>2</sub>·4H<sub>2</sub>O was 0.2 mmol, 0.3 mmol, 0.4 mmol and 0.6 mmol, respectively. Furthermore, NiCo-HMs-3/PTCN and NiCo-HMs-3/PBCN are obtained by replacing PCN with PTCN or PBCN and keeping the same reaction condition.

**1.7 Preparation of Ni(OH)<sub>2</sub>/PCN and Co(OH)<sub>2</sub>/PCN:** The preparation method was similar to that of (NiCo-HMs-x/PCN). The only difference was that only 0.2 mmol of Ni(CH<sub>3</sub>COO)<sub>2</sub>·4H<sub>2</sub>O or 0.4 mmol Co(CH<sub>3</sub>COO)<sub>2</sub>·4H<sub>2</sub>O was added during the preparation process. The resulting products were named as Ni(OH)<sub>2</sub>/PCN or

Co(OH)<sub>2</sub>/PCN.

### **1.8 Preparation of binary monolayer Ni-Co hydroxide monolayers (NiCo-HMs):**

The preparation method was similar to that of (NiCo-HMs-x/PCN). The only difference was that PCN was not added in the preparation process. The resulting dark gray product is denoted as NiCo-HMs.

### **1.9 Preparation of Ni-Co layered double hydroxides (NiCo-LDHs)/PCN hybrids**

**(NiCo-LDHs-3/PCN):** The method was developed based on the reported literature.<sup>1</sup>

Typically, 75 mg PCN, 0.4 mmol Ni(NO<sub>3</sub>)<sub>2</sub>·6H<sub>2</sub>O and 0.2 mmol Co(NO<sub>3</sub>)<sub>2</sub>·6H<sub>2</sub>O were dissolved in 37.5 mL ethylene glycol and 5.0 mL deionized water. The solution was stirred at room temperature for 30 mins, and then 3 mmol urea was added to the above solution and treated in an oil bath at 90 °C for 4 h. The precipitate was centrifuged and washed with distilled water and ethanol and finally dried under vacuum at 60°C. Finally, a gray-green product (denoted as NiCo-LDHs-3/PCN) was obtained.

**1.10 Preparation of Ni-Co layered double hydroxides (NiCo-LDHs):** The preparation method was similar to that of (NiCo-LDHs-3/PCN). The only difference was that PCN was not added in the preparation process. The resulting green product was denoted as NiCo-LDHs.

## **2. Characterization.**

The surface zeta potential of the samples was measured by using a ZS90 (Malvern Panalytical) device. A powder X-ray diffraction (XRD-6000, shimadzu), Fourier-transform infrared spectroscopy (Nicolet iS50) and ESCALAB 250XI (Thermo system)

X-ray photoelectron spectroscopy (XPS) were used to analyze the crystalline phases and chemical compositions of the samples. A NovaNano 450 (FEL) scanning electron microscopy (SEM) and JEM-2100HR transmission electron microscopy (TEM) apparatus were utilized for morphological investigation. Atomic force microscopy (AFM, Bruker, multimode8) images of NiCo-HMs were obtained to determine its thicknesses. N<sub>2</sub> adsorption/desorption was performed on NOVA3000e fully automated specific surface and pore size distribution analyzer device, and specific surface area and pore size distribution were obtained using Brunauer-Emmet-Teller (BET) and Barrett-Joyner-Halenda (BJH) models, respectively. Optical absorption properties were measured on a Shimadzu UV-2600 spectrophotometer. Photoluminescence (PL) and time-resolved photoluminescence (TRPL) spectra were recorded on a QuaanmansterTM40 spectrophotometer (Photonics International inc.) with an excitation wavelength of 365 nm. Static water contact angles were captured with a contact angle goniometer (DSC-100) at room temperature. For electron paramagnetic resonance (EPR) measurements, a Bruker A300 instrument was used with 2,2,6,6-Tetramethylpiperidinoxy (TEMPO, 0.1M) and 5,5-dimethyl-1-pyrroline-N-oxide (DMPO, 0.1M) as the spin-trapping agent to trap the reactive species including electrons and hydroxyl radical ( $\cdot\text{OH}$ ) radical, respectively.

### **3. Photocatalytic H<sub>2</sub> generation test.**

Photocatalytic H<sub>2</sub> generation experiments were conducted in a 100 mL three-necked flask reaction cell (19 mm\*3) under the illumination with 420 nm LED light

source. Typically, 20 mg sample was added to 80 mL aqueous solution comprising 10 vol% triethanolamine solution (10 vol% TEOA). The reactant mixture suspension was sonicated for 5 minutes and purged with high purity nitrogen for 15 minutes prior to each reaction. The evolved H<sub>2</sub> content was determined using a GC-2014 (Shimadzu) gas chromatograph equipped with a thermal conductivity detector. The apparent quantum efficiency (AQE) of HER was checked via the equation:

$$AQE (\%) = \frac{2 \times \text{amount of } H_2 \text{ molecules evolved in unit time}}{\text{number of incident photons in unit time}} \times 100\%$$

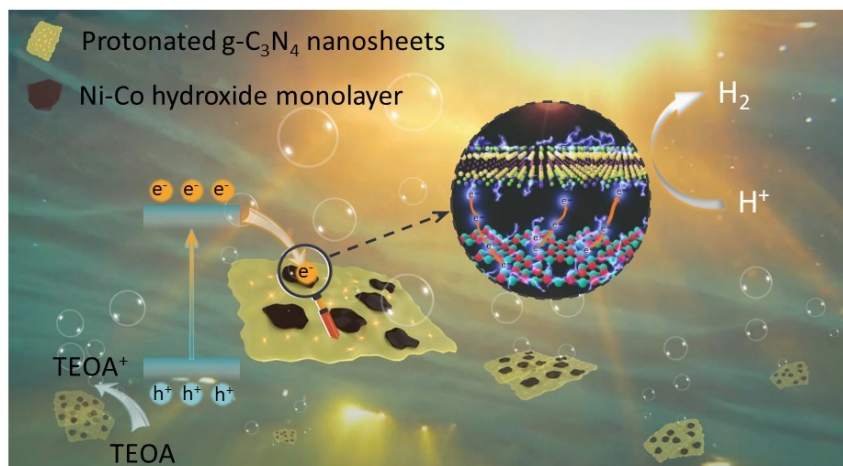
#### **4. Photoelectrochemical measurements.**

The photoelectrochemical performance of the samples (including instantaneous photocurrent response, EIS profiles and model-Schottky plots) were performed using a CHI 760E (CH Instruments) electrochemical analyzer equipped with a standard three-electrode system in which the platinum foil, Ag/AgCl and the sample were used as reference, counter and working electrodes, respectively.

#### **5. Computational details.**

All the spin-polarized calculations are performed using the projector augmented wave (PAW) pseudopotentials as implemented in the Vienna ab initio simulation package (VASP) code.<sup>2,3</sup> The generalized gradient approximation of Perdew-Burke-Ernzerhof parameterization (GGA-PBE).<sup>4</sup> During the structural optimization, 500 eV energy cutoff and 6×6×1 k-points are both adopted for Co(OH)<sub>2</sub> surface and Ni(OH)<sub>2</sub> surface supercells. The 9×9×1 k-points are applied for the electronic property

calculations. All geometry are adequately optimized until the convergence criteria for energy and force are less than  $1 \times 10^{-5}$  eV and  $0.01$  eV/Å, respectively. Here a thickness of  $20$  Å vacuum was selected in the z direction to avoid periodic interactions.



**Scheme S1** Possible mechanism for photocatalytic HER with NiCo-HMs/PCN.

Note: During visible-light irradiation, the electrons of PCN are stimulated and leap to CB. Due to the intimate and large interface between the 2D NiCo-HMs and 2D PCN, the photogenerated electrons would transfer to NiCo-HMs cocatalyst to participate in  $\text{H}_2$  evolution. In particular, NiCo-HMs with synergistic Ni-Co active sites can act as an "electron transfer bridge" to facilitate photogenerated charge transfer. Meanwhile, the low  $\text{H}^*$  adsorption energy of NiCo-HMs is favour for the reduction of  $\text{H}_2\text{O}$  to  $\text{H}_2$  by photogenerated electrons, leading to a greatly enhanced HER efficiency.

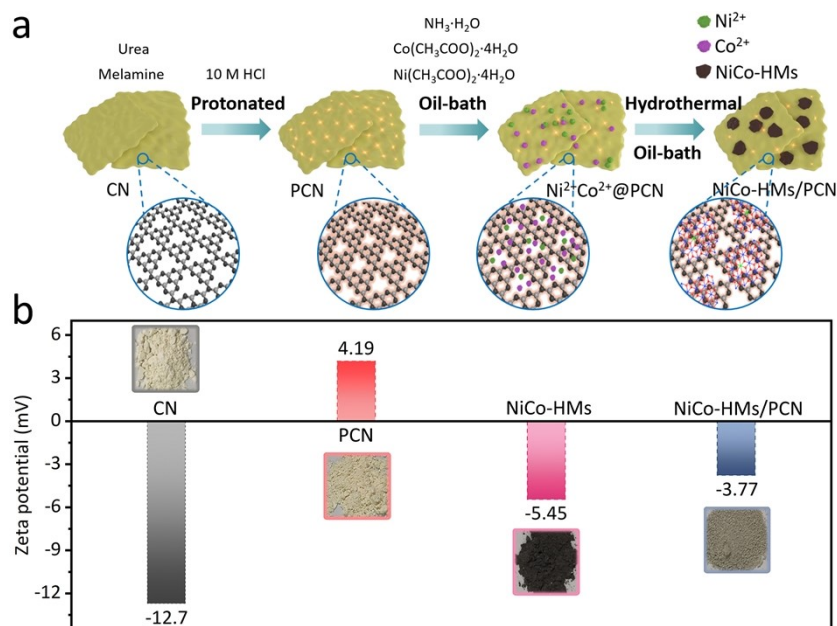


**Fig. S1** (a) Schematic process of NiCo-HMs-3/PCN hybrids and (b) the corresponding zeta potential of different samples during synthesis.

Note: The zeta potential measurement can demonstrate the surface charge modification of CN. As expected, the zeta potential changed from negative (-12.7 mV) to positive (+4.19 mV) when the CN was treated with HCl solution, indicating successful preparation PCN.<sup>5</sup> The zeta potential measured for NiCo-HMs-3/PCN was -3.77 mV.

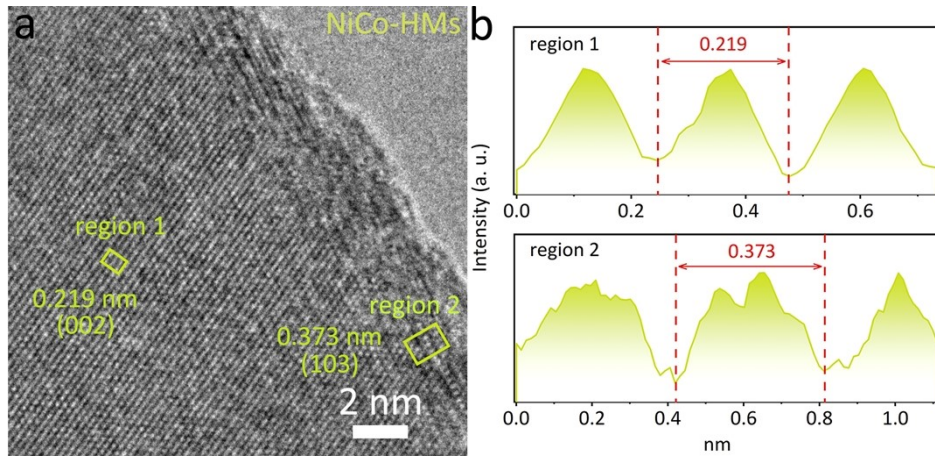


**Fig. S2** (a) The HRTEM image and (b) the lattice spacing of corresponding region of NiCo-HMs.

Note: As shown in Fig. S2a, two important regions are selected (region 1 and region 2) to calibrate the lattice parameters. By measuring the distances between the peaks and valleys of the lattice stripes (Fig. S2b), the lattice spacings of region 1 and region 2 were determined to be 0.219 and 0.213 nm, respectively, corresponding to (002) and (103) crystal planes of NiCo-HMs.

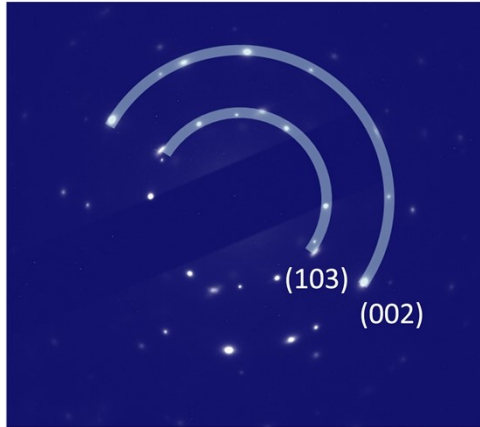


**Fig. S3** The SAED pattern of pure NiCo-HMs.

Note: As shown in Fig. S3, SAED pattern was used to further confirm that the exposed crystal planes of NiCo-HMs were (002) and (103) planes.

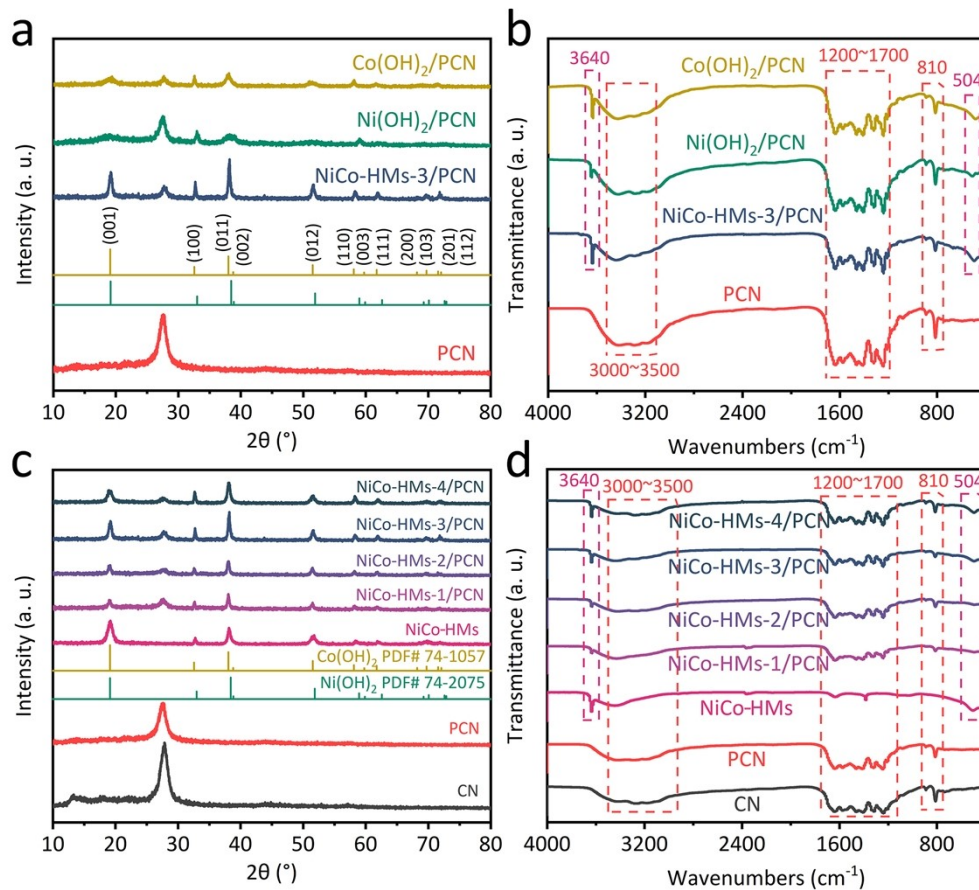


**Fig. S4** (a) The XRD patterns and (b) FT-IR spectra of different samples. (c) The XRD patterns and (d) FT-IR spectra of NiCo-HMs-x/PCN hybrids.

Note: As shown in Fig. S4a, the XRD peaks of the prepared NiCo-HMs with different crystalline planes show typical features of the  $\beta$ -phase,<sup>6</sup> indicating the successful synthesis of NiCo-HMs. Furthermore, NiCo-HMs-x/PCN samples were proved to be successfully prepared via XRD results (Fig. S4c). In detail, the peaks at  $27.3^\circ$  and  $13.1^\circ$  correspond to the interlayer stacking of periodic tri-s-triazine units and the triangular N-bonds of aromatic structures with in-plane repeating motifs, respectively.<sup>7</sup>

In Fig. S4b and S4d, the FT-IR spectra show that the absorption bands at wave number  $810\text{ cm}^{-1}$  are from the vibrational mode of tri-s-triazine, indicating the presence

of NH/NH<sub>2</sub> based melon units. Several strong absorption bands located in the range of 1200-1700 cm<sup>-1</sup> are caused by the stretching vibrations of the C-N heterocycle in aromatic PCN. The signals at 3000-3500 cm<sup>-1</sup> are attributed to the vibrational modes of the residual amino N-H.<sup>8</sup> For the composite samples, besides those peaks belonging to the g-C<sub>3</sub>N<sub>4</sub> are observed, two other peaks ascribed to the respiration modes of Co/Ni-O-H in NiCo-HMs and O-H in the β-phase of NiCo-HMs are observed at 504 cm<sup>-1</sup> and 3640 cm<sup>-1</sup>, which signals the existence of hydroxides in NiCo-HMs-x/PCN samples.<sup>9,10</sup>

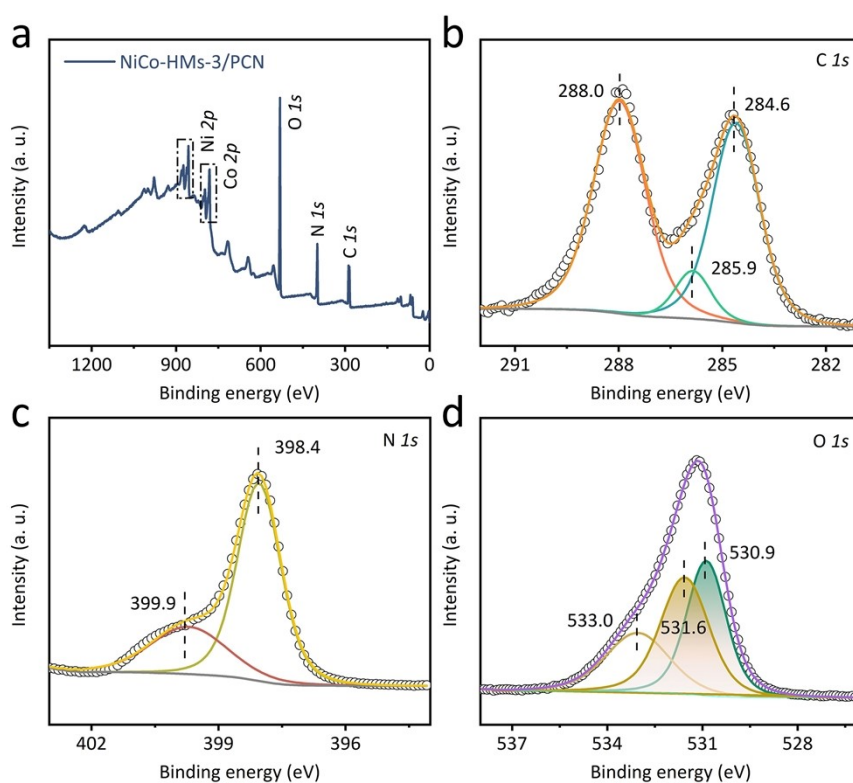


**Fig. S5** X-ray photoelectron spectroscopy (XPS): (a) survey profile and (b) C 1s, (c) N 1s and (d) O 1s of NiCo-HMs-3/PCN.

Note: As shown in Fig. S5a, the survey spectrum showed C, N, O, Ni, and Co elements. In the C 1s region (Fig. S5b), three peaks appeared at 284.6, 285.9 and 288.8 eV, respectively. The peak at 284.6 eV was caused by the  $sp^2$  hybridized C-C bond; and the peaks at 285.9 and 288.8 eV were attributed to the C-N coordination and N-C=N coordination of PCN, respectively. Meanwhile, the binding energy peaks of the N 1s at 398.4 and 399.9 (Fig. S5c) were corresponded to the C=N-C bond and N-(C)<sub>3</sub> group, respectively.<sup>11</sup> In Fig. S5d, the O 1s spectrum was fitted to three peaks at 530.9, 531.6, and 533.0 eV, which can be ascribed to Ni-O-H, Co-O-H, and possibly absorbed hydroxyl groups, respectively.<sup>12</sup>

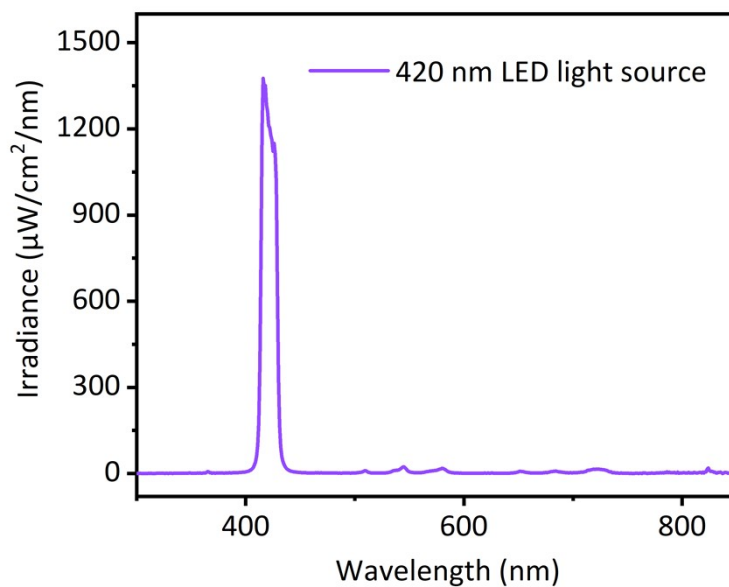


**Fig. S6** The irradiance spectrum of 80 W LED light source with 420 nm filter.

Note: As shown in Fig. S6, only the light accumulated at 420 nm can pass through the optical filter and be used for the exciting light for photocatalysis, indicating that NiCo-HMs-3/PCN is a visible-light photocatalyst.

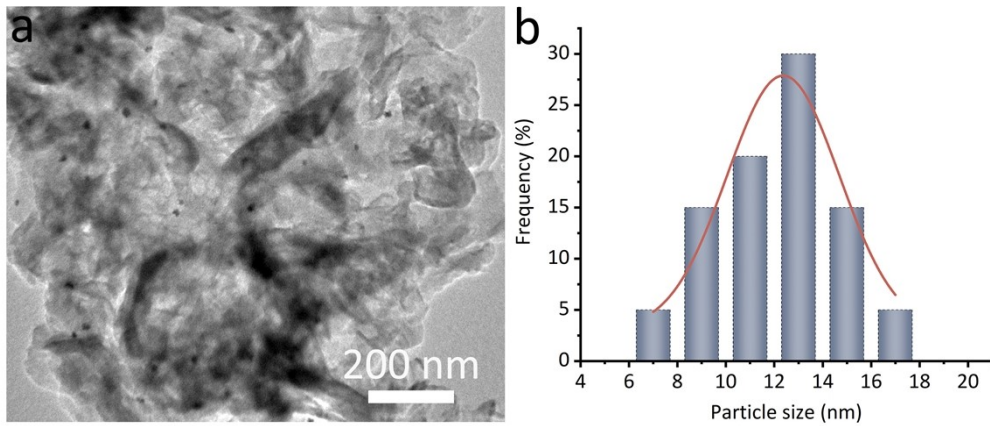


**Fig. S7** (a) The TEM image of 1% Pt<sub>NP</sub>/PCN and (b) the corresponding size distribution of Pt NPs.

Note: As shown in Fig. S7a, homogeneous Pt nanoparticles (NPs) anchored on PCN can be clearly found. Meanwhile, the sizes of Pt NPs are mostly concentrated at 13 nm (Fig. S7b). This result illustrates the successful preparation of Pt<sub>NP</sub>/PCN.

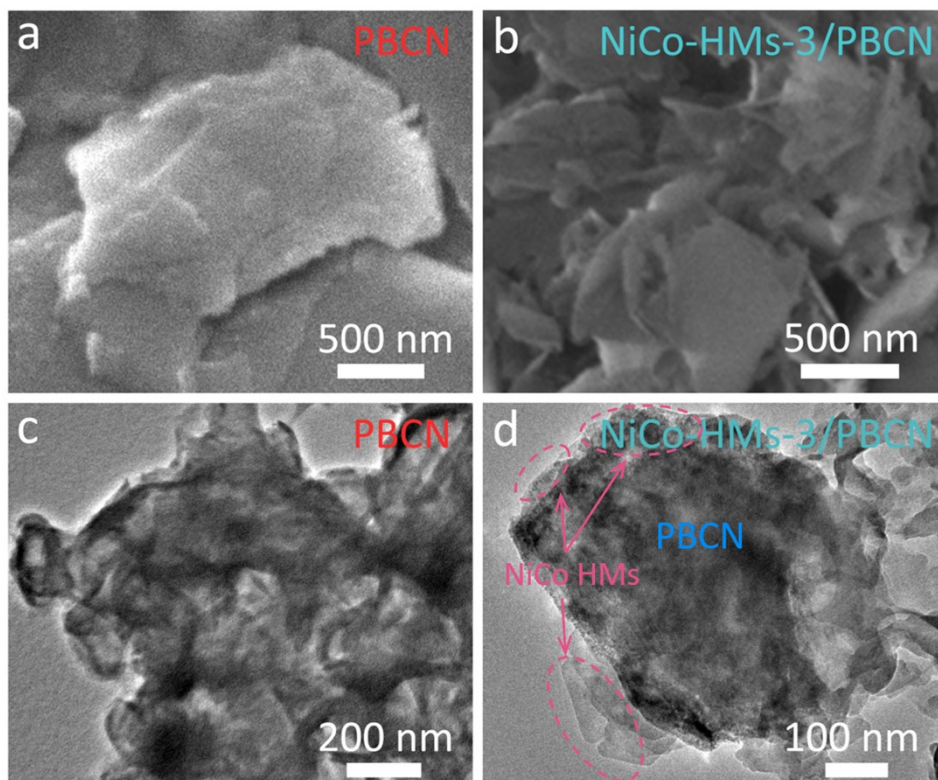


**Fig. S8** The SEM images of (a) PBCN and (b) NiCo-HMs-3/PBCN. The TEM images of (c) PBCN and (d) NiCo-HMs-3/PBCN.

Note: NiCo-HMs-3/PBCN was synthesized by substituting PCN with PBCN and utilizing the same preparation procedure as NiCo-HMs-3/PCN, as illustrated in Fig. S8. The bulk architectures of PBCN and NiCo-HMs-3/PBCN are confirmed in Fig. S8a and S8b, respectively. Especially, compared to PBCN (Fig. S8c), it can be found that NiCo-HMs are anchored to the PBCN (Fig. S8d), demonstrating the successful fabrication of NiCo-HMs-3/PBCN.

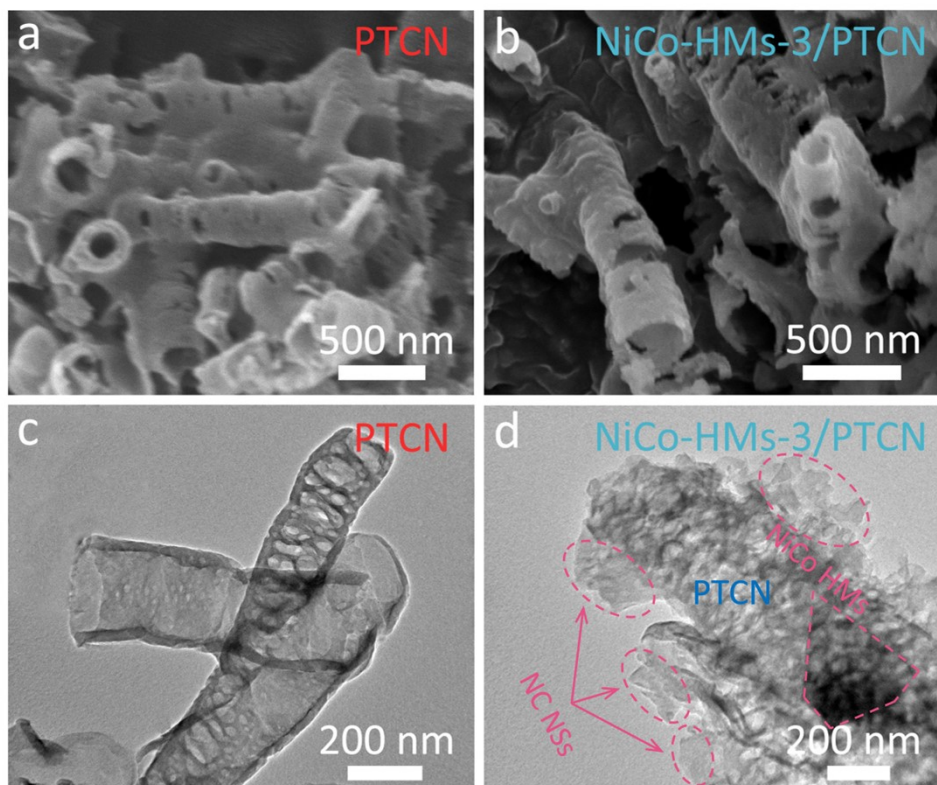


**Fig. S9** The SEM images of (a) PTCN and (b) NiCo-HMs-3/PTCN. The TEM images of (c) PTCN and (d) NiCo-HMs-3/PTCN.

Note: NiCo-HMs-3/PTCN was synthesized by substituting PCN with PTCN and utilizing the same preparation procedure as NiCo-HMs-3/PCN, as illustrated in Fig. S9. The tubular architectures of PTCN are confirmed in Fig. S9a and S9b, respectively. Especially, compared to PTCN (Fig. S9c), NiCo-HMs are anchored to the PTCN tubular (Fig. S9d), demonstrating the successful fabrication of NiCo-HMs-3/PTCN.

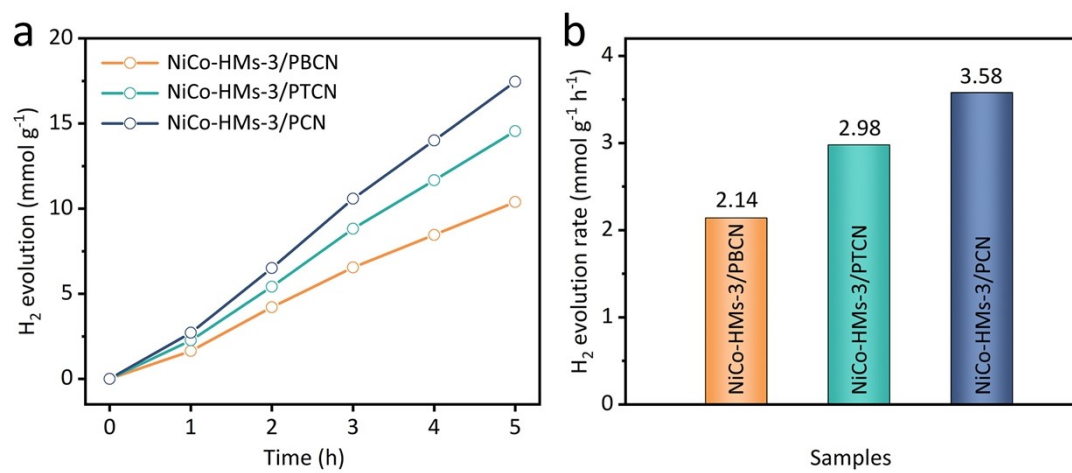


**Fig. S10** (a) Time course of H<sub>2</sub> evolution and (b) photocatalytic H<sub>2</sub>-evolved rate of the samples with different morphologies.

Note: As shown in Fig. S10, the photocatalytic HER activity rates of NiCo-HMs-3/PBCN, NiCo-HMs-3/PTCN and NiCo-HMs-3/PCN are 2.14 mmol g<sup>-1</sup> h<sup>-1</sup>, 2.98 mmol g<sup>-1</sup> h<sup>-1</sup> and 3.58 mmol g<sup>-1</sup> h<sup>-1</sup>, respectively.

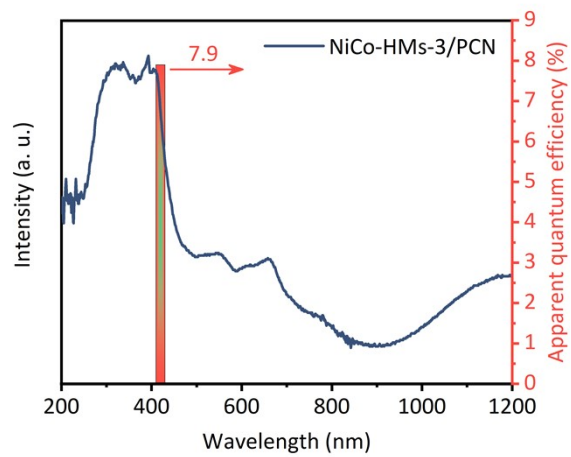


**Fig. S11** AQE measurement of NiCo-HMs-3/PCN.

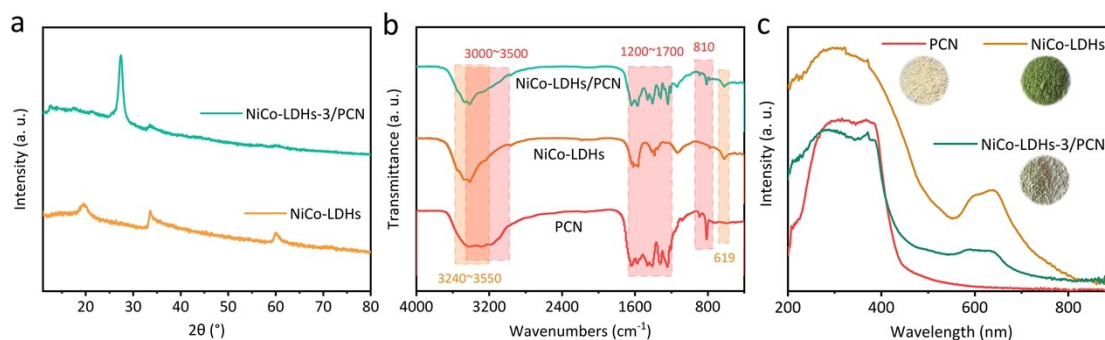


**Fig. S12** The (a) XRD patterns, (b) FT-IR spectra and (c) UV-Vis DRS spectra of PCN, NiCo-LDHs and NiCo-LDHs-3/PCN.

Note: As shown in Fig. S12a, the XRD peaks at  $2\theta = 10.1^{\circ}$ ,  $19.7^{\circ}$ ,  $33.8^{\circ}$ , and  $60.1^{\circ}$  were corresponded to the (003), (006), (009), and (110) planes of the prepared NiCo-LDHs, indicating the successful synthesis of NiCo-LDHs (JCPDS No. 33-0429).

In Fig. S12b, the FT-IR spectra show that the absorption bands at wavenumber of  $810 \text{ cm}^{-1}$  are ascribed to the vibrational mode of tri-s-triazine, indicating the presence of NH/NH<sub>2</sub> based melon units. Moreover, several strong absorption bands located in the range of  $1200\text{-}1700 \text{ cm}^{-1}$  are caused by the stretching vibrations of the C-N heterocycle in aromatic PCN. In addition, the wide spectral band between  $3240\text{-}3550 \text{ cm}^{-1}$  is attributed to the O-H stretching vibration from adsorbed/interlayer water molecules which have formed Ni/Co-OH groups and the peak at  $619 \text{ cm}^{-1}$  originates from Ni/Co-OH stretching vibrations.<sup>13</sup>

The UV-vis DRS (Fig. S12c) of the as-prepared samples exhibit the similar absorption band edge at about 420 nm, indicating that the deposition of NiCo-LDHs cocatalyt would not change the band structure of the PCN. Note that an evident enhancement in the absorption could be observed for the NiCo-LDHs/PCN sample in the region around 600 nm.<sup>14</sup>

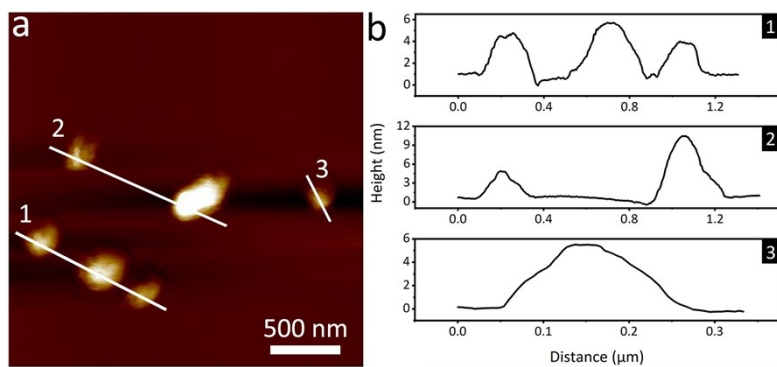


**Fig. S13** (a) AFM image and (b) corresponding height profile of NiCo-LDHs.

Note: The AFM image (Fig. S13) indicated that the thickness of NiCo-LDHs was about 4-10 nm, suggesting the multilayer structure of NiCo-LDHs.

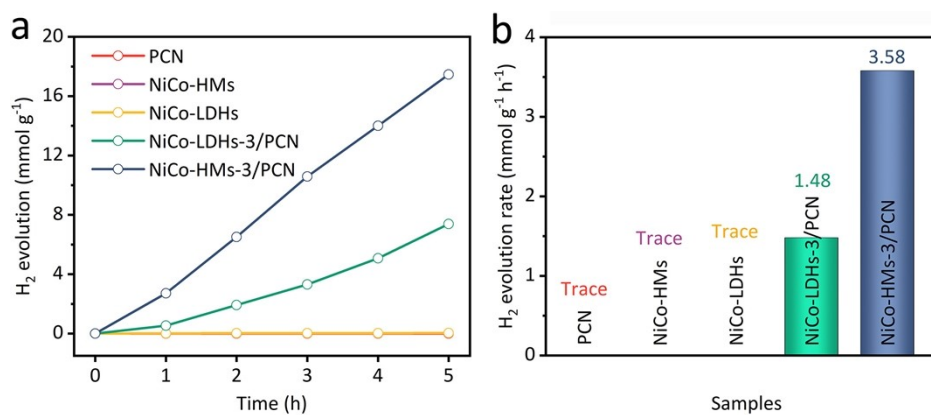


**Fig. S14** (a) Time course of H<sub>2</sub> evolution and (b) photocatalytic H<sub>2</sub>-evolved rate over different samples.

Note: The photocatalytic activity of prepared samples was evaluated under a light-emitting diode (LED, 80 W, 420 nm) light source. As expected, the pristine PCN, NiCo-HMs and NiCo-LDHs produced only trace of H<sub>2</sub>, while with NiCo-HMs and NiCo-LDHs as cocatalysts, the H<sub>2</sub> generation rate of NiCo-HMs/PCN and NiCo-LDHs/PCN significantly increased to 3.58 mmol g<sup>-1</sup> h<sup>-1</sup> and 1.48 mmol g<sup>-1</sup> h<sup>-1</sup>, respectively (Fig. S14), indicating the better cocatalytic effect of NiCo-HMs with monolayer structure.

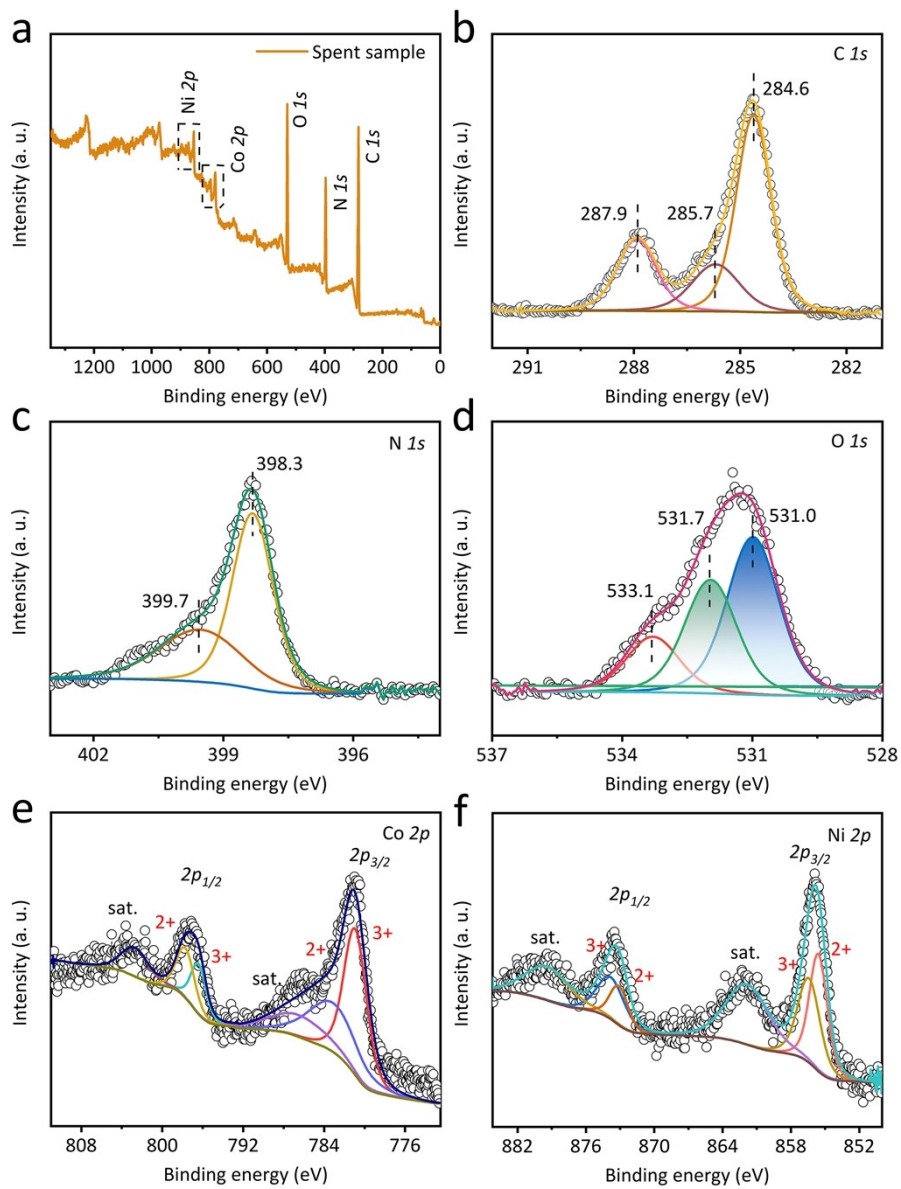


**Fig. S15** XPS spectra: (a) survey profile and (b) C 1s, (c) N 1s, (d) O 1s, (e) Co 2p and (f) Ni 2p of NiCo-HMs-3/PCN spent sample.

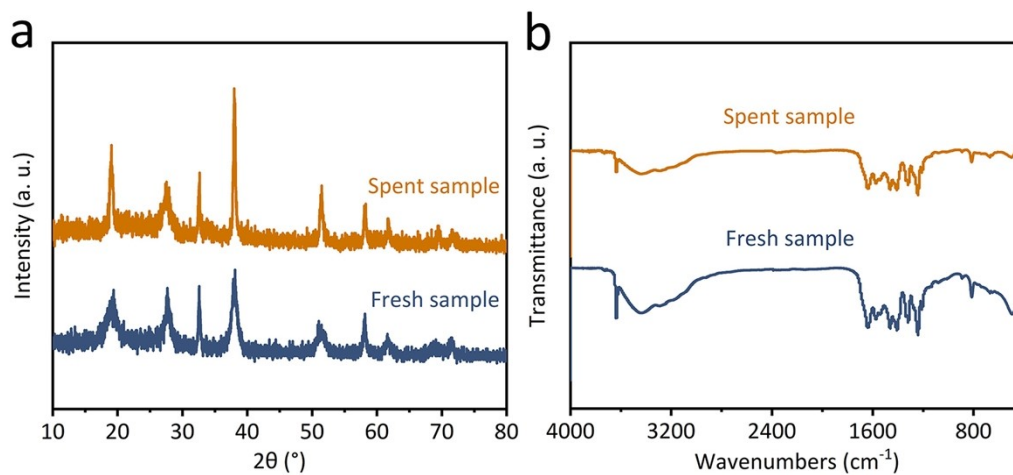


**Fig. S16** (a) XRD patterns and (b) FT-IR spectra of fresh sample and spent sample.

Note: As shown in Fig. S16, both the XRD pattern (Fig. S16a) and FT-IR spectrum (Fig. S16b) of the spent NiCo-HMs-3/PCN matched well with the fresh sample, effectively verifying the excellent chemical stability of NiCo-HMs-3/PCN.<sup>15</sup>

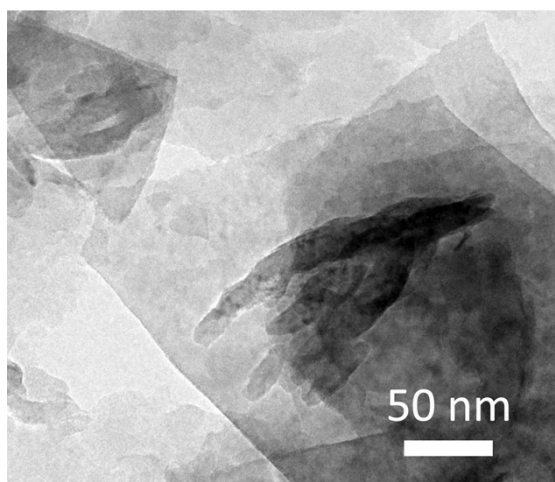


**Fig. S17** The TEM image of spent sample of NiCo-HMs-3/PCN.

Note: As shown in Fig. S17, the morphology of the spent sample presents a mixture of nanosheets, which is similar to that of the fresh sample.

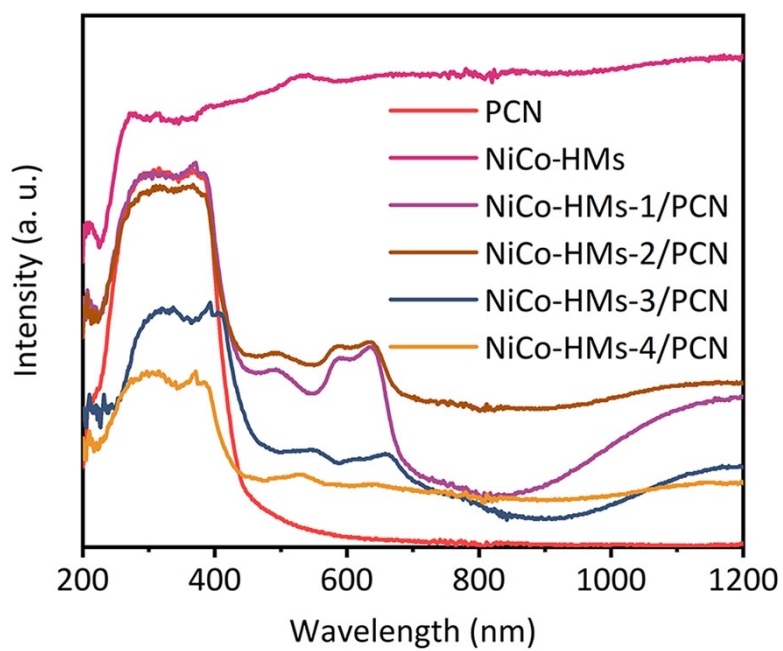


**Fig. S18** DRS spectra of NiCo-HMs-x/PCN.

Note: Compared to PCN, the NiCo-HMs-x/PCN composites demonstrate much higher light absorption capacity in the visible region.

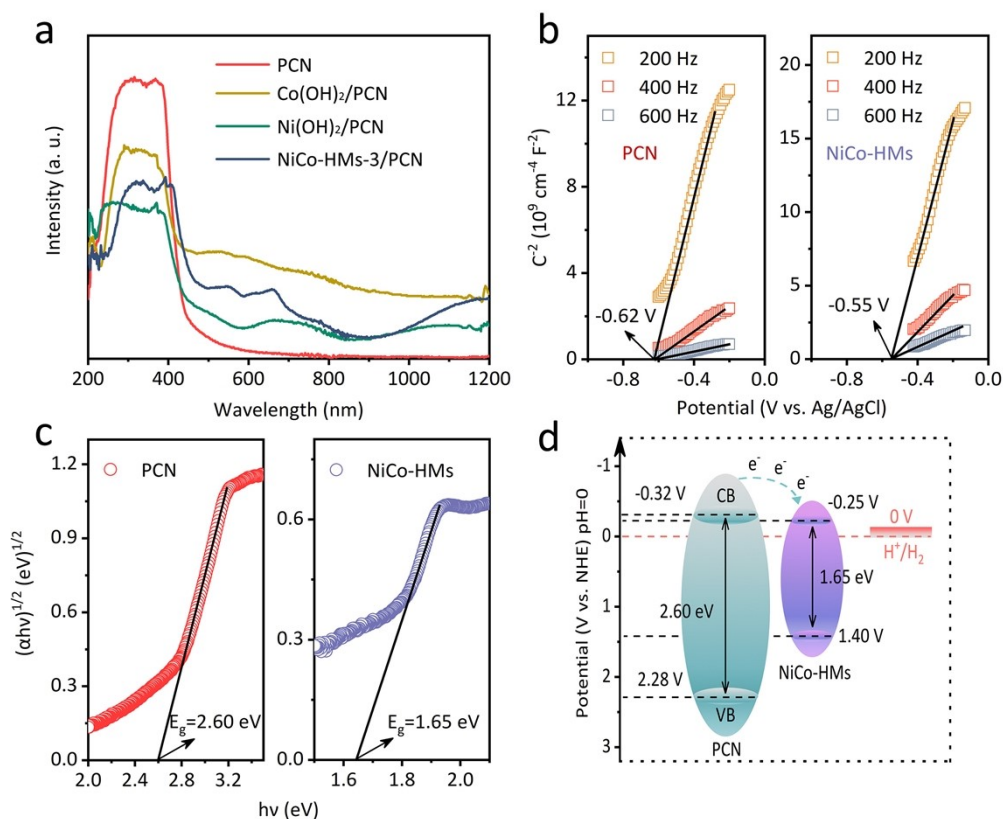


**Fig. S19** (a) DRS spectra of different samples. (b) The Mott-Schottky (M-S) plots of PCN and NiCo-HMs-3/PCN. (c) Band gaps of PCN and NiCo-HMs. (d) Schematic illustration of band structure and charge transfer in the NiCo-HMs-3/PCN hybrids.

Note: As illustrated in Fig. S19a, the absorption edge of pristine PCN is positioned at about 420 nm. The light absorption capacity of NiCo-HMs-3/PCN is greatly increased and the absorption edge is expanded to around 500 nm. In Fig. S19b, the flat-band potentials of PCN and NiCo-HMs are -0.62 and -0.55 V, respectively. The values of  $E_{fb}$  are calculated to be -0.02 V and 0.05 V (vs. NHE, pH = 0) based on the formula:

$$E_{fb} \text{ (vs. NHE)} = E_{Ag/AgCl} + 0.059 \times pH + E_{Ag/AgCl}^{\theta} \text{ (pH} = 6.8, E_{Ag/AgCl}^{\theta} = 0.197)$$

Generally, the conduction band ( $E_{CB}$ ) of n-type semiconductor is 0.3 V more negative than its  $E_{fb}$ . Therefore, the  $E_{CB}$  of PCN and NiCo-HMs are estimated at -0.32 and -0.25

V. Furthermore, the energy gap ( $E_g$ ) of PCN and NiCo-HMs are 2.60 V and 1.65V from DRS spectra (Fig. S19c). In addition, according to the equation:  $E_g = E_{VB} - E_{CB}$ , the values of conduction band ( $E_{VB}$ ) of PCN and NiCo-HMs are determined to be 2.28 V and 1.40 V (vs. NHE, pH = 0), respectively.<sup>16</sup> The energy level matching relationships between NiCo-HMs and PCN have been described in Fig. S19d.

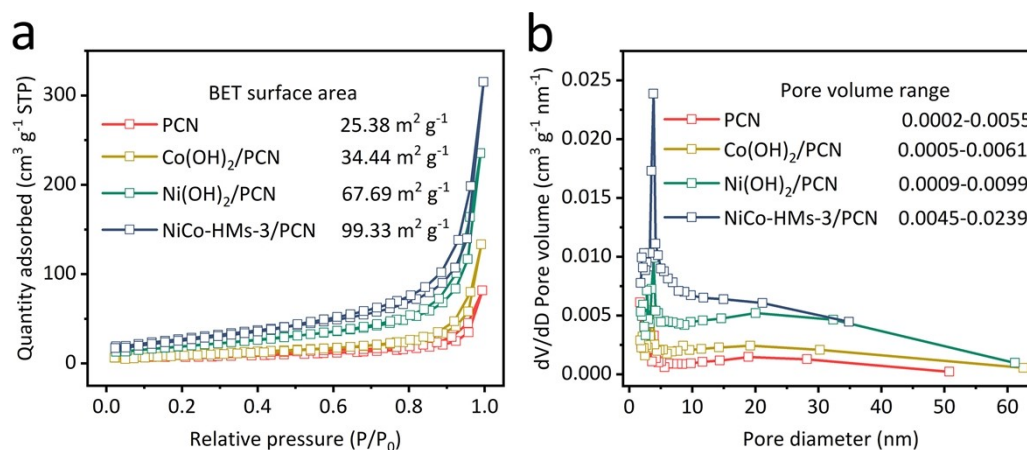


**Fig. S20** (a) N<sub>2</sub> adsorption–desorption isotherms and (b) the Barrett–Joyner–Halenda (BJH) pore size distributions of different samples.

Note: As shown in Fig. S20a, the BET surface area of PCN, Co(OH)<sub>2</sub>/PCN, Ni(OH)<sub>2</sub>/PCN and NiCo-HMs-3/PCN are 25.38, 34.44, 67.69 and 99.33 m<sup>2</sup> g<sup>-1</sup>, respectively. The BET surface area of NiCo-HMs-3/PCN is almost four times larger than that of PCN, indicating that the NiCo-HMs-3/PCN exhibits more active sites. Moreover, in Fig. S20b, the pore volume size of the NiCo-HMs-3/PCN is larger than that of the PCN, confirming that NiCo-HMs-3/PCN may possess stronger adsorption capacity.<sup>17</sup> The larger surface area and pore volume size of the NiCo-HMs-3/PCN are favor to enhance the photocatalytic HER.

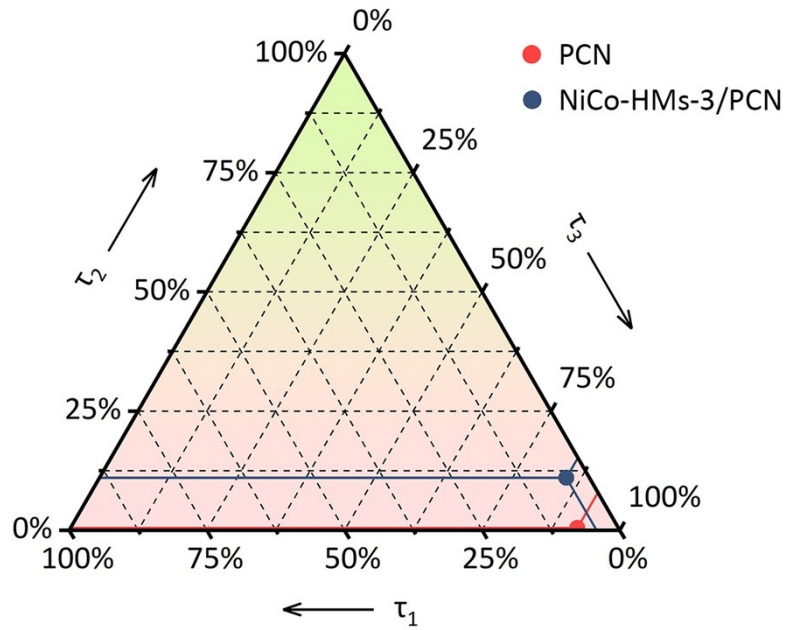


**Fig. S21** Schematic representation of the positive decay components of PCN and NiCo-HMs-3/PCN.

Note: As shown in Fig. S21, three positive decay components of  $\tau_1$ ,  $\tau_2$ , and  $\tau_3$  of PCN are 10.84 ns, 0.68 ns and 133.71 ns, which account the proportion of 7.46%, 0.46% and 92.07%, respectively. However, for NiCo-HMs-3/PCN,  $\tau_1$ ,  $\tau_2$ , and  $\tau_3$  are 0.36 ns, 0.94 ns and 7.24 ns, which account the proportion of 7.46%, 0.46% and 92.07%, respectively. Notably, the proportion of  $\tau_2$  in NiCo-HMs-3/PCN is much higher than that in PCN.

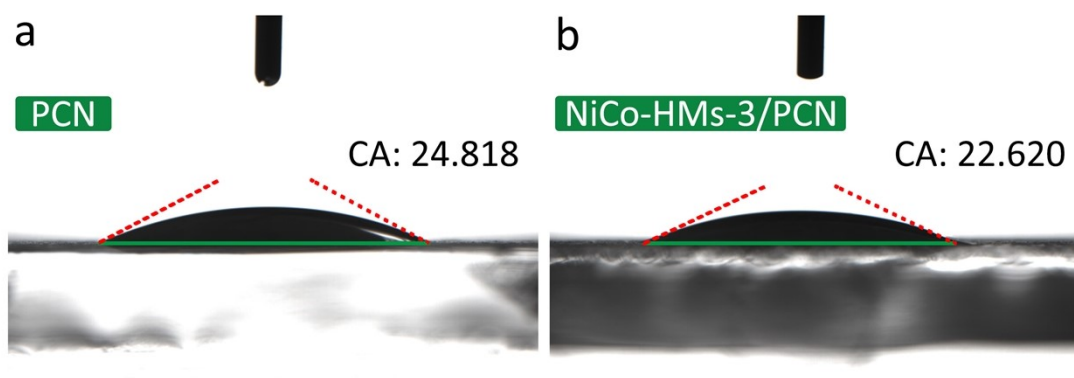


**Fig. S22** Contact angle of (a) PCN and (b) NiCo-HMs-3/PCN with water.

Note: As shown in Fig. S22, the contact angles (CA) of PCN and NiCo-HMs-3/PCN are  $24.818^\circ$  and  $22.620^\circ$ , respectively. The smaller contact angle of the NiCo-HMs-3/PCN means the surface of the NiCo-HMs-3/PCN can be more easily wetted with water.<sup>18</sup>

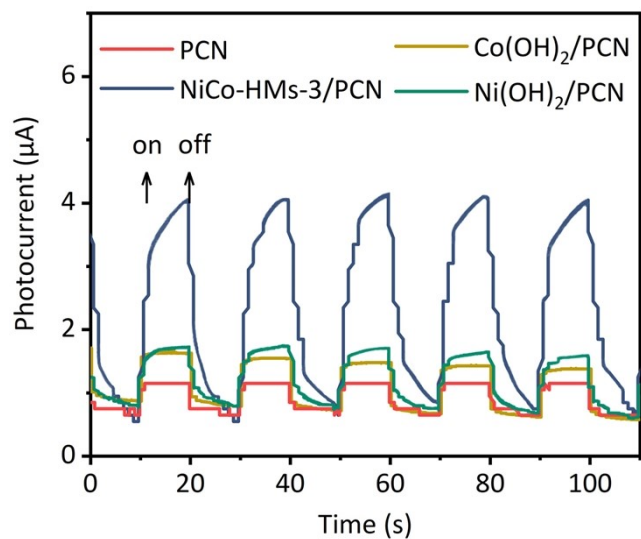


**Fig. S23** Transient photocurrent response of the PCN,  $\text{Co(OH)}_2/\text{PCN}$ ,  $\text{Ni(OH)}_2/\text{PCN}$  and  $\text{NiCo-HMs-3/PCN}$  samples.

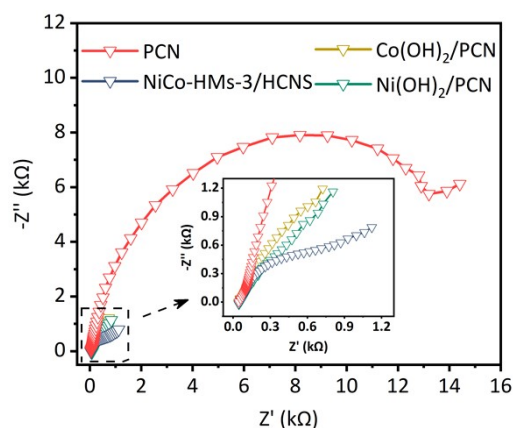


**Fig. S24** The EIS Nyquist plots of the PCN,  $\text{Co(OH)}_2/\text{PCN}$ ,  $\text{Ni(OH)}_2/\text{PCN}$  and NiCo-HMs-3/PCN samples.

Samples	PCN	$\text{Co(OH)}_2/\text{PCN}$	$\text{Ni(OH)}_2/\text{PCN}$	NiCo-HMs-3/PCN
$R_{ct}$ (kΩ)	24.46	7.98	3.98	0.89
Error (%)	5.90	21.72	29.02	4.79

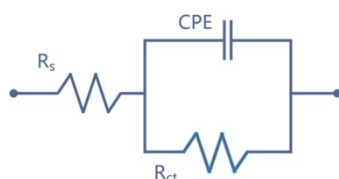


**Fig. S25** The fitted results of impedance spectra for PCN,  $\text{Co(OH)}_2/\text{PCN}$ ,  $\text{Ni(OH)}_2/\text{PCN}$  and NiCo-HMs-3/PCN.

Note: As shown in Fig. S25 the equivalent circuit contains a solution resistor ( $R_s$ ), a constant phase element (CPE) and a charge transfer resistor ( $R_{ct}$ ). The fitted results of  $R_{ct}$  of PCN,  $\text{Co(OH)}_2/\text{PCN}$ ,  $\text{Ni(OH)}_2/\text{PCN}$  and NiCo-HMs-3/PCN are 24.46 kΩ, 7.98 kΩ, 3.98 kΩ and 0.89 kΩ, respectively. Moreover, the error of fitted results are also exhibited, they are all within the correctable range.

**Table S1** The specific value of XPS high-resolution spectrum peaks and content of Ni 2p and Co 2p for NiCo-HMs-3/PCN.

Peaks (eV)	Species	Content (%)
781.2	Co <sup>3+</sup> 2p <sub>3/2</sub>	37.58
784.2	Co <sup>2+</sup> 2p <sub>3/2</sub>	9.70
786.4	sat.	22.88
796.7	Co <sup>3+</sup> 2p <sub>1/2</sub>	6.34
798.3	Co <sup>2+</sup> 2p <sub>3/2</sub>	7.35
802.9	sat.	16.15
855.8	Ni <sup>2+</sup> 2p <sub>3/2</sub>	19.55
857.5	Ni <sup>3+</sup> 2p <sub>3/2</sub>	17.19
861.9	sat.	35.85
873.3	Ni <sup>2+</sup> 2p <sub>1/2</sub>	8.45
875.2	Ni <sup>3+</sup> 2p <sub>3/2</sub>	7.80
879.7	sat.	11.16

**Table S2** A brief comparison of HER performance of photocatalysts reported in the literatures.

Year	Catalysts	Sacrificial agent	H <sub>2</sub> evolution rate (mmol g <sup>-1</sup> h <sup>-1</sup> )	Ref.
2022	NiCo-HMs/PCN	10 vol% TEOA	3.58	<b>This work</b>
2022	NiS/P-g-C <sub>3</sub> N <sub>4</sub>	20 vol% TEOA	1.50	19
2022	NiS/Cd <sub>0.5</sub> Zn <sub>0.5</sub> S/g-C <sub>3</sub> N <sub>4</sub>	10 vol% TEOA	6.77	20
2022	Ni/NiS/g-C <sub>3</sub> N <sub>4</sub>	15 vol% TEOA	0.52	21
2021	CoS/g-C <sub>3</sub> N <sub>4</sub> /EY	15 vol% TEOA	1.91	22
2020	gC <sub>3</sub> N <sub>4</sub> /PPy/CoS/Co(OH) <sub>2</sub>	10 vol% TEOA	0.93	23
2020	Ni(OH) <sub>2</sub> /g-C <sub>3</sub> N <sub>4</sub>	10 vol% TEOA	0.92	24
2020	Ni-MoS <sub>x</sub> /g-C <sub>3</sub> N <sub>4</sub>	10 vol% TEOA	5.97	25
2019	CoP/g-C <sub>3</sub> N <sub>4</sub>	10 vol% TEOA	0.30	26
2019	NiCo <sub>2</sub> O <sub>4</sub> /g-C <sub>3</sub> N <sub>4</sub>	20 vol% TEOA	5.48	27
2019	Ni <sub>2</sub> P/g-C <sub>3</sub> N <sub>4</sub>	10 vol% TEOA	0.89	28
2019	Pt/Ni(OH) <sub>2</sub> -C <sub>3</sub> N <sub>4</sub>	- (Pure water)	3.01	29
2018	BP QDs/g-C <sub>3</sub> N <sub>4</sub>	10 vol% Methanol	1.9	30
2018	CoS <sub>x</sub> /g-C <sub>3</sub> N <sub>4</sub>	20 vol% TEOA	0.63	31
2017	NiCoP@NiCo-Pi/g-C <sub>3</sub> N <sub>4</sub>	10 vol% TEOA	0.53	32
2017	Ni <sub>x</sub> Co <sub>y</sub> /g-C <sub>3</sub> N <sub>4</sub>	10 vol% TEOA	0.55	33
2014	g-C <sub>3</sub> N <sub>4</sub> /NiS	10 vol% TEOA	0.45	34

**Table S3** The specific value of XPS high-resolution spectrum peaks and content of Ni 2p and Co 2p for NiCo-HMs-3/PCN spent sample.

Peaks (eV)	Species	Content (%)
781.1	Co <sup>3+</sup> 2p <sub>3/2</sub>	39.54
784.0	Co <sup>2+</sup> 2p <sub>3/2</sub>	11.09
785.8	sat.	24.02
796.6	Co <sup>3+</sup> 2p <sub>1/2</sub>	8.02
798.2	Co <sup>2+</sup> 2p <sub>3/2</sub>	9.26
802.7	sat.	8.07
855.7	Ni <sup>2+</sup> 2p <sub>3/2</sub>	21.23
856.4	Ni <sup>3+</sup> 2p <sub>3/2</sub>	19.02
861.8	sat.	26.01
873.1	Ni <sup>2+</sup> 2p <sub>1/2</sub>	11.59
875.3	Ni <sup>3+</sup> 2p <sub>3/2</sub>	7.29
879.4	sat.	14.85

## References

1. M. Rashidimoghaddam, A. Saljooqi, T. Shamspur and A. Mostafavi, *New J. Chem.*, 2020, **44**, 15584.
2. G. Kresse and J. Furthmüller, *Phys. Rev. B*, 1996, **54**, 11169.
3. G. Kresse and J. Furthmüller, *Comp. Mater. Sci.*, 1996, **6**, 15-50.
4. G. Kresse and J. Furthmüller, *Phys. Rev. B*, 1999, **59**, 1758.
5. Y. Liu, M. He, R. Guo, Z. Fang, S. Kang, Z. Ma, M. Dong, W. Wang and L. Cui, *Appl. Catal. B Environ.*, 2020, **260**, 118137.
6. J. Yan, H. Wu, H. Chen, L. Pang, Y. Zhang, R. Jiang, L. Li and S. Liu, *Appl. Catal. B Environ.*, 2016, **194**, 74-83.
7. L. Cui, J. Song, A. F. McGuire, S. Kang, X. Fang, J. Wang, C. Yin, X. Li, Y. Wang and B. Cui, *ACS Nano*, 2018, **12**, 5551-5558.
8. L. Shen, G. Lei, Y. Fang, Y. Cao, X. Wang and L. Jiang, *Chem. Commun.*, 2018, **54**, 2475.
9. S. Gao, Y. Sun, F. Lei, L. Liang, J. Liu, W. Bi, B. Pan and Y. Xie, *Angew. Chem. Int. Ed.*, 2014, **53**, 12789-12793.
10. E. Vivek, A. Arulraj, M. Khalid and I. Vetha Potheher, *Inorg. Chem. Commun.*, 2021, **130**, 108704.
11. H. Bian, Y. Ji, J. Yan, P. Li, L. Li, Y. Li and S. Frank Liu, *Small*, 2018, **14**, 1703003.
12. J. Zhang, S. Shao, D. Zhou, T. Di and T. Wang, *ACS Appl. Energy Mater.*, 2021, **4**, 6340-6347.
13. J. Zou, D. Xie, J. Xu, X. Song, X. Zeng, H. Wang and F. Zhao, *Appl. Surf. Sci.*, 2022, **571**, 151322.
14. M. Zhang, Z. Luo, M. Zhou, G. Zhang, K. A. Alamry, L. A. Taib, A. M. Asiri and X. Wang, *Appl. Catal. B Environ.*, 2017, **210**, 454-461.
15. P. Dong, Y. Wang, A. Zhang, T. Cheng, X. Xi and J. Zhang, *ACS Catal.* 2021, **11**, 13266-13279.
16. X. Yu, H. Su, J. Zou, Q. Liu, L. Wang and H. Tang, *Chin. J. Catal.*, 2022, **43**, 421-432.
17. X. Zhang, Y. Guo, J. Tian, B. Sun, Z. Liang, X. Xu and H. Cui, *Appl. Catal. B Environ.*, 2018, **232**, 355-364.
18. J. Zhang, Y. Li, X. Zhao, L. Wang, H. Chen, S. Wang, X. Xu, L. Shi, L.-C. Zhang, Y. Zhu, H. Zhang, Y. Liu, G. Nealon, S. Zhang, M. Wu, S. Wang and H. Sun, *Nano Energy*, 2021, **89**, 106357.
19. D. Sun, T. Zhou, G. Che and C. Liu, *Appl. Surf. Sci.*, 2022, **578**, 152004.
20. J. Song, S. Huang and Y. Su, *ACS Appl. Energy Mater.*, 2022, **5**, 1414-1420.
21. Z. Fan, X. Guo, Z. Jin, X. Li and Y. Li, *Langmuir*, 2022, **38**, 3244-3256.
22. J. Li, B. Luo, X. Zheng, D. Jing and L. Ma, *Catal. Sci. Technol.*, 2021, **11**, 7624-7631.
23. K. Li, Y.-Z. Lin, K. Wang, Y. Wang, Y. Zhang, Y. Zhang and F.-T. Liu, *Appl. Catal. B Environ.*, 2020, **268**, 118402.

24. Q. Hao, Y. Song, Z. Mo, J. Deng, J. Yi, W. El-Alami, H. Xu and H. Li, *Solar RRL*, 2020, **4**, 1900538.
25. B. Wang, X. Li, H. Wu, G. Xu, X. Zhang, X. Shu, J. Lv and Y. Wu, *ChemCatChem*, 2020, **12**, 911-916.
26. C. Han, T. Zhang, Q. Cai, C. Ma, Z. Tong and Z. Liu, *J. Am. Ceram. Soc.*, 2019, **102**, 5484-5493.
27. W. Chang, W. Xue, E. Liu, J. Fan and B. Zhao, *Chem. Eng. J.*, 2019, **362**, 392-401.
28. R. Boppella, W. Yang, J. Tan, H.-C. Kwon, J. Park and J. Moon, *Appl. Catal. B Environ.*, 2019, **242**, 422-430.
29. S. Sun, Y.-C. Zhang, G. Shen, Y. Wang, X. Liu, Z. Duan, L. Pan, X. Zhang and J.-J. Zou, *Appl. Catal. B Environ.*, 2019, **243**, 253-261.
30. L. Kong, Y. Ji, Z. Dang, J. Yan, P. Li, Y. Li and S. F. Liu, *Adv. Funct. Mater.*, 2018, **28**, 1800668.
31. J. Fu, C. Bie, B. Cheng, C. Jiang and J. Yu, *ACS Sustainable Chem. Eng.*, 2018, **6**, 2767-2779.
32. Z. Qin, Y. Chen, Z. Huang, J. Su and L. Guo, *J. Mater. Chem. A*, 2017, **5**, 19025-19035.
33. J. Wen, J. Xie, H. Zhang, A. Zhang, Y. Liu, X. Chen and X. Li, *ACS Appl. Mater. Interfaces*, 2017, **9**, 14031-14042.
34. Z. Chen, P. Sun, B. Fan, Z. Zhang and X. Fang, *J. Phys. Chem. C*, 2014, **118**, 7801-7807.